

# **Developing diffusion imaging for accurate image representation**

- A Report submitted as the examined component of the Project Module SXP390 -

By Justin Ferguson

C5510989

September 3, 2019

# Abstract

Diffusion MRI (dMRI) has been developed since 1965 as a popular medical imaging technique to detect water flow abnormalities within cellular structures and their surrounding environments. In this review, Fick's laws of diffusion and the physics of MRI are investigated and then combined to form signal equations to model diffusing water molecules.

The evolution of this report shows two flavours of dMRI, both are dependent upon the compartmental tissue structures that enclose the moving water molecules. To model their flux within these environments, a special  $3 \times 3$  matrix is defined, the diffusion tensor. When all nine components are expanded, an equation in the form of an ellipsoid is procured. This is used as a model to describe direction-restricted diffusion, such as in axon bundles within the brain. A special case of this equation describes a sphere, which is naturally used to model unrestricted diffusion in open compartments, such as cerebrospinal fluid (CSF).

In this review, two popular dMRI measures, mean diffusivity (MD) and fractional anisotropy (FA), are described and their viability as accurate imaging techniques are assessed. Diffusion tensor imaging (DTI) tractography is also introduced and is seen to evolve naturally from FA. The review closes with some general considerations, supplemented by a list of recommendations an operator should follow in order to achieve optimum dMRI accuracy.

# Contents

<b>1</b>	<b>Introduction</b>	<b>3</b>
<b>2</b>	<b>Understanding diffusion</b>	<b>5</b>
2.1	Fick's first law and the diffusion tensor . . . . .	5
2.2	Isotropic diffusion . . . . .	7
2.3	Anisotropic diffusion . . . . .	8
2.4	Fick's second law and the probability density functions . . . . .	9
<b>3</b>	<b>MRI and diffusion imaging</b>	<b>11</b>
3.1	Proton nuclear magnetic resonance . . . . .	11
3.2	The Boltzmann distribution and the magnetisation vector . . . . .	12
3.3	Magnetic field gradients and pulse sequences . . . . .	13
3.4	The signal equations of dMRI . . . . .	15
<b>4</b>	<b>Introducing, comparing and contrasting popular imaging measures</b>	<b>17</b>
4.1	Introducing some imaging measures of dMRI . . . . .	17
4.2	Comparing and contrasting imaging measures . . . . .	19
<b>5</b>	<b>General considerations to improve accuracy</b>	<b>23</b>
5.1	Optimising the $b$ -value . . . . .	23
5.2	Magnetic field strength and SNR . . . . .	24
5.3	Increasing gradient pulse angular resolution . . . . .	24
<b>6</b>	<b>Conclusion</b>	<b>25</b>
	<b>References</b>	<b>27</b>

# Introduction

Diffusion magnetic resonance imaging (dMRI) is a technique used in medical pathology to diagnose unusual water flow within tissue structures. The idea takes advantage of the random molecular motion of water in these regions, to image fluid transport and provide structural information. Diffusion MRI is a robust imaging technique, particularly for detecting the onset of cerebral infarction. However, with its versatility comes increasing complexity. It is therefore easy to neglect the level of accuracy required as a medical tool, in the wake of advancing diffusion techniques.

The central theme of this project is to critically review and evaluate dMRI research, with emphasis on testing and improving diffusion imaging accuracy in different diagnostic procedures. Each discussed method increases sequentially in complexity, but is coupled with the potential for greater imaging accuracy.

The project objectives are as follows:

1. Illustrate the theory of diffusion and MRI as a prerequisite towards diffusion imaging.
2. Describe the characteristics and phenomena of isotropic and anisotropic diffusion imaging.
3. Report on popular diffusion MRI measures and discuss their viability as accurate imaging techniques.
4. Explore methods to improve dMRI accuracy as proposed by the academic community.
5. Create a set of guidelines for an operator to follow to optimise dMRI accuracy.

The scope of this project will cover all the relevant theory required to describe dMRI signal equations. Once defined, two popular measures, fractional anisotropy (FA) and mean diffusivity (MD) are introduced. Their viability as accurate imaging techniques is then explored. A discussion then follows to describe possible ways of improving their accuracy. Finally, a set of guidelines are created to aid dMRI image accuracy in the conclusion.

The discussion in this project evolves around the research performed in relevant peer-reviewed articles, such as Feldman et al. (2010) and Mukherjee et al. (2003). Literature was found by using academic search engines, mainly Web of Science and Science Direct. Appropriate articles were then narrowed using Booleans. Other papers were found by following citation trails and by using the ‘cited by’ feature, available on most academic search engines. A balance between using older, highly cited papers and newer papers was struck.

# Understanding diffusion

## 2.1 Fick's first law and the diffusion tensor

The experimental observations of Fick (1855) describe the phenomenon of diffusion. The following are important points drawn from his observations:

1. A local high concentration of substance within a fluid medium will uniformly flow to its surrounding regions of lower concentration. This movement is said to be driven by the gradient itself.
2. A net flux will continue until both regions have the same concentration.

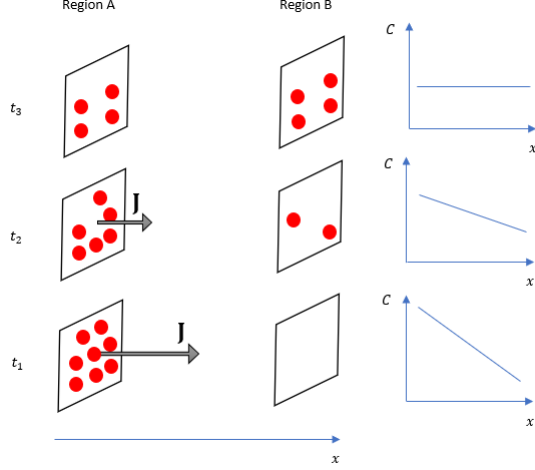
To summarise, diffusion flux is proportional to a negative linear concentration gradient. The details of this motion are eloquently encapsulated within Fick's first law. Note, for all further discussion, assume the concentration,  $C$ , is position and time dependent.

$$\mathbf{J} = -D\nabla C \tag{2.1.1}$$

In this equation,  $\mathbf{J}$  is the flux density (i.e. flux per unit area) in units  $\text{mol m}^{-2} \text{s}^{-1}$  and  $\nabla C$  is the concentration gradient in units  $\text{mol m}^{-4}$ . The minus sign indicates the direction of flow - from high to low concentration. The proportionality constant,  $D$ , is the diffusion coefficient (or diffusivity) unique to the substance. It is the rate of diffusion (in units  $\text{m}^2 \text{s}^{-1}$ ) and varies according to absolute temperature, particle size and fluid viscosity (Einstein, 1905). Figure 2.1 shows Fick's first law in action for one-dimensional diffusion, at three separate times.

Figure 2.1: Fick's first law

visualised in one-dimension. At  $t_1$ , the particle difference between the two regions is great. Over time, the concentrations will slowly level off, which corresponds to a decreasing  $\mathbf{J}$  and increasing  $\nabla C$ .



Diffusion is a three-dimensional phenomenon, so it is insightful to present Fick's first law as a matrix equation.

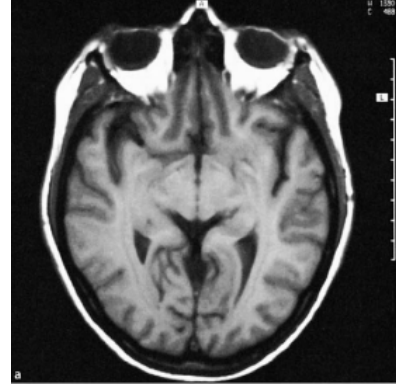
$$\begin{bmatrix} J_x \\ J_y \\ J_z \end{bmatrix} = -D \begin{bmatrix} \frac{\partial C}{\partial x} \\ \frac{\partial C}{\partial y} \\ \frac{\partial C}{\partial z} \end{bmatrix} \quad (2.1.2a)$$

$$= - \begin{bmatrix} D & 0 & 0 \\ 0 & D & 0 \\ 0 & 0 & D \end{bmatrix} \begin{bmatrix} \frac{\partial C}{\partial x} \\ \frac{\partial C}{\partial y} \\ \frac{\partial C}{\partial z} \end{bmatrix} \quad (2.1.2b)$$

Hence, the diffusion coefficient has now been transformed into the symmetric diffusion tensor,  $\mathbf{D}$ . In diffusion magnetic resonance imaging, decoding the elements of  $\mathbf{D}$  from a resonance signal is required to form an image. Signals are acquired from  $\text{H}^+$  (bare hydrogen) bound in water, where they are most abundant (Plewes and Kucharczyk, 2012). Within the brain, water diffusion occurs primarily in cerebrospinal fluid (CSF), intracellular and intercellular space (Huisman, 2010).

CSF is contained within open structures such as the ventricles, cranial and spinal subarachnoid spaces (Sakka et al., 2011). Within these environments, water is allowed to diffuse unhindered. Conversely, white brain matter is compact (Crichton and Ward, 2013) and restricts diffusion in certain directions. As a consequence, an MRI image can be obtained to show contrast between the regions (figure 2.2). These differences are now discussed in more detail.

Figure 2.2: A magnetic resonance image revealing the structure of the brain. The liquorice black regions within the cranium are compartments of CSF. This is contrasted by white regions of dense brain tissue. Credit to Reiser et al. (2008).

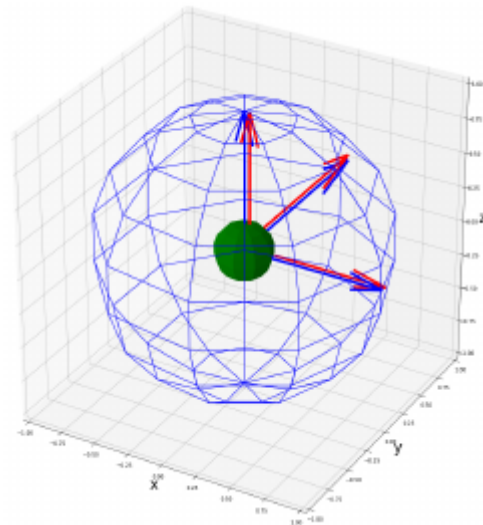


## 2.2 Isotropic diffusion

Water in CSF diffuses in the traditional manner observed by Fick (1855), i.e. a slow, but equal flow in all directions. It is therefore not favoured towards any particular direction. Diffusion of this sort is said to be isotropic. With the inclusion of  $\mathbf{D}$ , equations 2.1.2a and 2.1.2b show the components of  $-\nabla C$  need not equal  $\mathbf{J}$ . However, their directions must remain the same. Moreover, as a consequence of spherical symmetry, the vector components are rotationally invariant about any choice of basis.

Rotational invariance is a property of diagonal symmetry in the diffusion tensor. This special form of  $\mathbf{D}$  is an eigenstate and its elements are the eigenvalues  $\lambda_1 = \lambda_2 = \lambda_3 = D$ , corresponding to the linearly independent eigenvectors  $\epsilon_1$ ,  $\epsilon_2$  and  $\epsilon_3$ . Figure 2.3 shows a concentration of CSF in green and the projection of  $\mathbf{J}$  in three-dimensional space at a later time in blue. Note, the components of  $\mathbf{J}$  (blue arrows) and  $-\nabla C$  (red arrows) are in the same directions and parallel to the axes.

Figure 2.3: Three-dimensional isotropic diffusion is spherical in shape due to symmetry. The eigenvalues here have been selected as  $\lambda_1 = \lambda_2 = \lambda_3 = 1 \text{ m}^2 \text{ s}^{-1}$  for simplicity.





## 2.3 Anisotropic diffusion

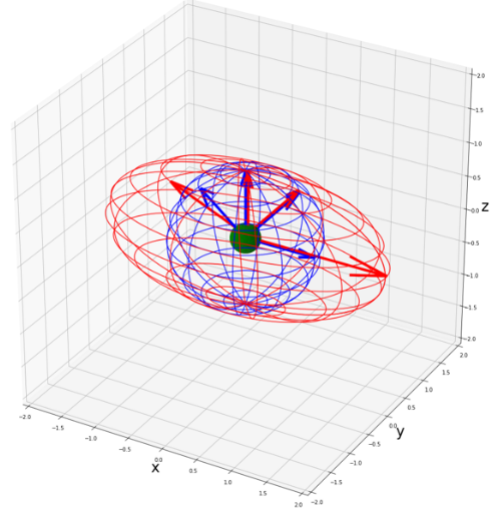
Water diffusion in white brain matter occurs mainly within microscopic axon bundles connected between brain tissue (Tournier, 2019). Individual axons are tubular in shape, their geometry restricts diffusion in the radial direction and favours it along the tubular axis. Diffusion has become anisotropic in this case (Moseley, 1991). The mathematics of anisotropic diffusion have been investigated by Crank (1975) and Bassler et al. (1994). The discussion ahead summarises this intuitively.

Consider an axon in which  $J_x$  is twice that of  $J_y$  and  $J_z$ , then equation 2.1.2b becomes

$$\begin{bmatrix} J_x \\ J_y \\ J_z \end{bmatrix} = -D \begin{bmatrix} 2 & 0 & 0 \\ 0 & 1 & 0 \\ 0 & 0 & 1 \end{bmatrix} \begin{bmatrix} \frac{\partial C}{\partial x} \\ \frac{\partial C}{\partial y} \\ \frac{\partial C}{\partial z} \end{bmatrix}. \quad (2.3.1)$$

Figure 2.4 shows the time-evolved projection of  $\mathbf{J}$  (in red) and  $-\nabla C$  (in blue) inside the axon. Note, the concentration gradient of the substance is projected evenly in all directions, but  $\mathbf{J}$  has an  $x$ -direction preference. Therefore, to satisfy equation 2.3.1, the projection of  $\mathbf{J}$  is a linear transformation of  $-\nabla C$  by  $\mathbf{D}$  into an ellipsoid shape. As a result,  $\mathbf{J}$  and  $-\nabla C$  are not aligned when pointing off-axis.

Figure 2.4: Three-dimensional anisotropic diffusion is represented by an ellipsoidal flux density. The orthogonal red/blue arrows are superposed along its principal axes. Rotation about these axes is invariant when parallel with the basis. For simplicity,  $D = 1 \text{ m}^2 \text{ s}^{-1}$ .



Anisotropic diffusion usually requires the full use of  $\mathbf{D}$ , transforming Fick's first law into

$$\begin{bmatrix} J_x \\ J_y \\ J_z \end{bmatrix} = - \begin{bmatrix} D_{xx} & D_{xy} & D_{xz} \\ D_{yx} & D_{yy} & D_{yz} \\ D_{zx} & D_{zy} & D_{zz} \end{bmatrix} \begin{bmatrix} \frac{\partial C}{\partial x} \\ \frac{\partial C}{\partial y} \\ \frac{\partial C}{\partial z} \end{bmatrix}. \quad (2.3.2)$$

$\mathbf{D}$  now describes the rotation of the ellipsoid in space and models diffusion in any orientation. For simplicity,  $\mathbf{D}$  is always assumed to be symmetric (Balluffi et al., 2005). Unlike a sphere, the ellipsoid will have rotational invariance only when the principle axes are aligned with the basis vectors. Therefore, a change in basis from Cartesian coordinates to the ellipsoid frame is usually required by using the rotation matrix  $\mathbf{R}$ . The eigenvectors are now superposed onto the new basis, enabling a diagonal matrix of eigenvalues,  $\mathbf{\Lambda}$ , to be found by diagonalisation.

$$\mathbf{\Lambda} = \mathbf{R}^T \mathbf{D} \mathbf{R} \quad (2.3.3)$$

These eigenvalues measure the *weight* of diffusion along the principal ellipsoid axes. An eigenvalue with the greatest *weighting* is assumed to have a diffusion preference along its eigenvector. This is always in the axial principal direction of the ellipsoid. It is the objective of diffusion tensor imaging (DTI) to find these eigenvalues to form an image.

## 2.4 Fick's second law and the probability density functions

A model to describe diffusion across a non-linear concentration gradient requires a second-order spatial derivative. This term is found by substituting equation 2.1.1 into the continuity equation, which is in essence, just the conservation of mass. A convenient form of the continuity equation is

$$\frac{\partial C}{\partial t} + \nabla \cdot \mathbf{J} = 0. \quad (2.4.1)$$

Substituting Fick's first law for isotropic and anisotropic diffusion into this equation produces two variants of Fick's second law. For isotropic diffusion,

$$\frac{\partial C}{\partial t} - D \nabla^2 C = 0. \quad (2.4.2)$$

Solving this equation produces the well known univariate Gaussian probability density function (PDF) (Balluffi et al., 2005),

$$C(r, t) = \frac{N}{\sqrt{4\pi Dt}} e^{-\frac{r^2}{4Dt}} \quad (t > 0), \quad (2.4.3)$$

where  $r$  is the radial coordinate and  $N$  is the number of diffusing particles. It is said to be univariate because it depends only upon one spatial coordinate, a consequence of spherical symmetry.

For anisotropic diffusion,

$$\frac{\partial C}{\partial t} - \nabla \cdot \begin{bmatrix} D_{xx} & D_{xy} & D_{xz} \\ D_{yx} & D_{yy} & D_{yz} \\ D_{zx} & D_{zy} & D_{zz} \end{bmatrix} \nabla C = 0. \quad (2.4.4)$$

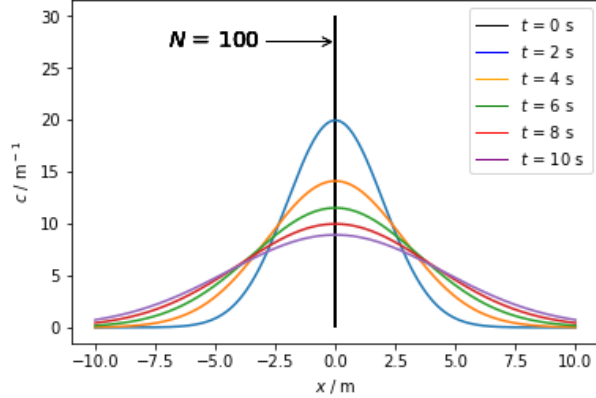
The solution to equation 2.4.4 has been extensively studied by Harville (2018), and a well excepted solution is the multivariate Gaussian PDF, introduced by Bassler et al. (1994). If the initial position of the particle distribution is located at the mean, the solution becomes

$$C(\mathbf{r}, t) = \frac{N}{(4\pi t)^{\frac{3}{2}} |\mathbf{D}|^{\frac{1}{2}}} e^{-\frac{\mathbf{r}^T \mathbf{D}^{-1} \mathbf{r}}{4t}} \quad (t > 0), \quad (2.4.5)$$

where  $\mathbf{r}^T = \begin{bmatrix} x & y & z \end{bmatrix}$ . The distribution is now said to be multivariate because it depends on all three spatial coordinates.

When integrated, the power of these equations is their ability to make probabilistic predictions about the spatial evolution of diffusion at discrete time intervals. Figure 2.5 shows the evolution of equation 2.4.3, from an impulse at  $x = 0$ , into its characteristic bell-shaped curve. For each step in time, the peak becomes broader and the function deviates over a wider region of space. This is consistent with observed diffusion and validates the Fickian model. Equations 2.4.3 and 2.4.5 will prove important in §3.4 for deriving dMRI signal equations.

Figure 2.5: The evolution of the univariate Gaussian PDF at discrete time intervals, for a distribution of 100 particles.



# MRI and diffusion imaging

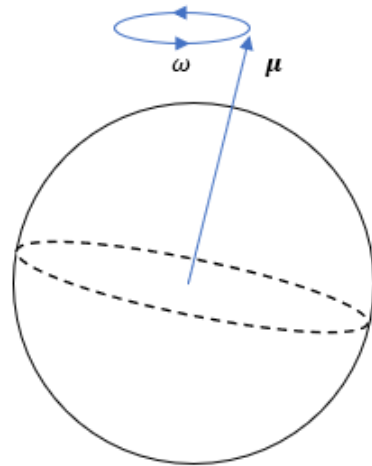
## 3.1 Proton nuclear magnetic resonance

An important property of  $\text{H}^+$  in nuclear magnetic resonance (NMR) is its degeneracy in an applied magnetic field,  $\mathbf{B}_0 (= B_0 \mathbf{e}_z, \text{by convention})$ . In this field, the magnetic moment will align itself with  $\mathbf{B}_0$  in a spin-up or spin-down state. The energy difference between these two states is,

$$\Delta E = \hbar \omega, \tag{3.1.1}$$

where  $\omega$  is the precessional Larmor frequency and  $\hbar$  is the reduced Planck constant. Photons of frequency  $\nu$  with energy  $\Delta E$  can be absorbed by a proton and cause a transition between states. From a classical perspective, this disturbance causes the proton to precess like a spinning top (figure 3.1).

Figure 3.1: Absorbed energy causes the magnetic moment  $\boldsymbol{\mu}$  of a proton to precess at frequency  $\omega$ .

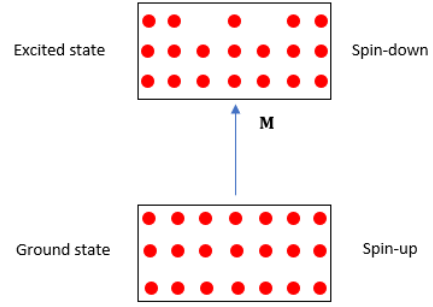


The gyromagnetic ratio  $\gamma$  of  $\text{H}^+$  causes  $\omega$  to fall within radio-frequency (RF) bandwidth. Hence, an RF pulse transmitted at  $\omega$  resonates with the proton, causing it to emit detectable radiation at the same frequency by spontaneous or stimulated emission. This is the basic NMR signal.

### 3.2 The Boltzmann distribution and the magnetisation vector

In reality, a single proton is too weak to be detected over background noise. Therefore, an NMR signal is made up from a vast number of weaker signals interfering constructively. The population of protons required to make these signals is modelled by a Boltzmann distribution (figure 3.2).

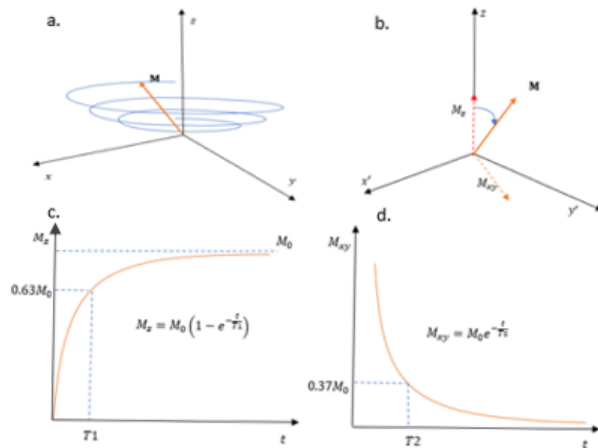
Figure 3.2: A Boltzmann distribution of protons displays a population difference. In this case, the magnetisation vector points towards the excited region.



In a Boltzmann distribution, there are always more spins in the ground state, which creates a population difference  $\Delta N$ . Hence, the overall effect of a transmitted RF pulse is to shift the population into a net excited state and reduce  $\Delta N$ . This difference is then restored by the emitted NMR signal a short time later.

$\Delta N$  is more often discussed in terms of a net magnetisation vector,  $\mathbf{M} = M_z \mathbf{e}_z$ . For protons, this vector points in the excited direction, the spin-down state. When an RF pulse excites  $\mathbf{M}$ , it will precess and gain a transverse component,  $M_{xy}$ , as shown in figure 3.3a. After the RF pulse,  $\mathbf{M}$  rotates back into its equilibrium position,  $\mathbf{M} = M_0 \mathbf{e}_z = M_z \mathbf{e}_z$ . During this relaxation process,  $\mathbf{M}$  induces a *free induction decay* NMR signal (figure 3.4) into a set of receivers located in the transverse plane.

Figure 3.3: a.  $\mathbf{M}$  precesses into the transverse plane by an RF pulse. b. The equivalent motion of  $\mathbf{M}$  as viewed from a rotational coordinate system about  $z$ . c. The recovery of  $M_z$  back to equilibrium. d. The decay of  $M_{xy}$  back to zero.



The recovery of  $\mathbf{M}$  is well described by the equations of Bloch (1946) and illustrated in figures 3.3c and 3.3d. After an exciting RF pulse,  $M_{xy}$  tends back to zero and  $M_z$  tends to  $M_0$ . This recovery process varies according to tissue type (figure 3.5). A pair of characteristic times for longitudinal and transverse relaxation,  $T1$  and  $T2$  respectively, are used as a means of identification.  $T1$  is the time taken for the absorbed energy to thermally dissipate into the spin system and increase  $M_z$  to  $0.63M_0$ .  $T2$  is the time taken for the spins to dephase and decrease  $M_{xy}$  to  $0.37M_0$ .

Figure 3.4: A free induction decay NMR signal. Credit to Hahn (1950a).

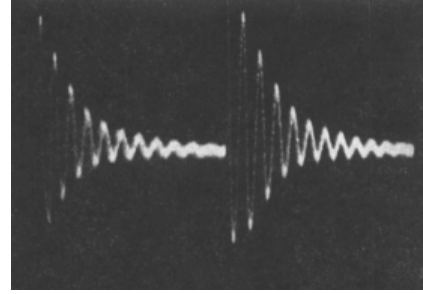


Figure 3.5: Tissue types are classified by  $T1$  and  $T2$ .

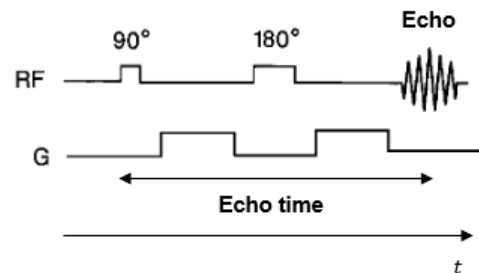
Credit to Plewes and Kucharczyk (2012).

Tissue	T1 (msec) 1.5T	T2 (msec)
Gray matter (41)	950	100
White matter (41)	600	80
Muscle (74)	900	50
Cerebrospinal fluid (CSF) (41)	4500	2200
Fat (41)	250	60
Blood (74)	~1400	~180-250

### 3.3 Magnetic field gradients and pulse sequences

In MRI, a rotating coordinate system like figure 3.3b is used to describe the rotation of  $\mathbf{M}$  from equilibrium. For example, a  $90^\circ$  RF pulse rotates  $\mathbf{M}$  completely into the  $x'y'$  plane. An RF pulse applied immediately afterwards rotates  $\mathbf{M}$   $180^\circ$  about  $x'$  back into the  $x'y'$  plane. A succession of pulses like this is a *pulse sequence*. In particular, the  $90^\circ$ - $180^\circ$  sequence (figure 3.6) produces the so-called spin-echo signal (Hahn, 1950b), in the form of an envelope wave.

Figure 3.6: The spin-echo pulse sequence. The  $90^\circ$  and  $180^\circ$  RF pulses are followed closely by the magnetic field pulse gradients,  $G$ . Modified from Neil (1997).



The very basics of MRI require a strong superconducting magnetic field,  $\mathbf{B}_0 = B_0 \mathbf{e}_z$ , and three orthogonal switching magnets to form a field gradient in any Cartesian direction. For a two-dimensional image, an area of tissue is isolated by creating three linear magnetic field gradients. These are referred to as slice-selection,  $G_s$ , frequency (or readout) encoding,  $G_f$ , and phase encoding,  $G_\phi$ . The gradients are mutually orthogonal, giving each spin its own unique Larmor frequency to resonate and emit a signal. These are then labelled by their spatial-frequencies  $k$  and plotted onto a two-dimensional grid,  $k$ -space (figure 3.7). The inverse Fourier transform of  $k$ -space then reveals the MRI image (figure 3.8).

Figure 3.7: The spatial frequencies  $k_x$  and  $k_y$  are obtained by rapidly switching  $G_f$  and  $G_\phi$  on and off in an image slice. The arrow indicates the direction of data acquisition. Credit to Huang et al. (2015).

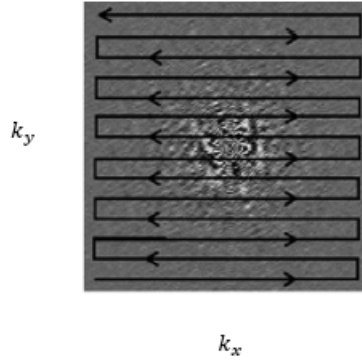
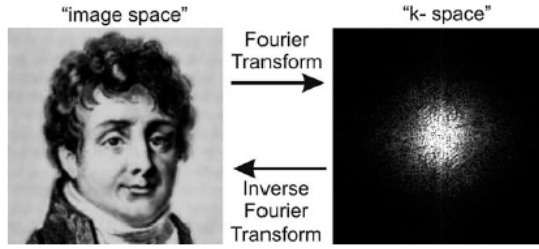
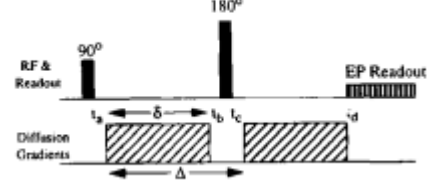


Figure 3.8: The Fourier transform from  $k$ -space to image space, and vice-versa. Credit to Plewes and Kucharczyk (2012).



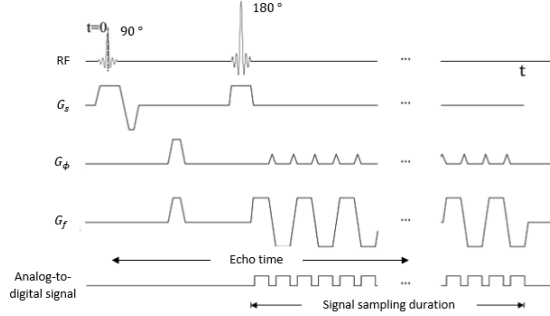
By applying the Bloch-Torrey equation for diffusing magnetisation (Torrey, 1956), Tanner and Stejskal (1965) modified the spin-echo sequence to incorporate a pair of steady magnetic field gradient pulses (figure 3.9),  $G_D$ , to image diffusing spins. As a result, if the echo signal intensity drops when compared to a baseline, the spins have acquired a net phase by diffusion. Conversely, if the signal remains constant, the spin phase has been unmodified by the pulses, implying diffusion restriction within the region. This is the fundamental theory behind a dMRI pulse sequence.

Figure 3.9: A pair of steady magnetic field gradient pulses. In this figure,  $\delta$  is the pulse duration and  $\Delta$  is the time taken from the beginning of the first pulse, to the start of the second. Credit to Alexander et al. (2006)



A hindrance of dMRI is image distortion due to patient motion. To overcome this problem, a fast pulse sequence was developed by Stehling et al. (1991). SS-EPI (single-shot echo-planar imaging) is similar to the spin-echo sequence and is used with dMRI because it traverses  $k$ -space in one pulse sequence (figure 3.10).

Figure 3.10: The SS-EPI pulse sequence. After the  $180^\circ$  RF pulse,  $G_f$  and  $G_\phi$  are rapidly switched on/off to produce many individual spin-echoes. This allows an entire region to be rapidly imaged. Modified from Brown (2014).



### 3.4 The signal equations of dMRI

A set of diffusion gradient pulses of magnitude  $G_x$  are set-up in the  $x$ -direction. If a spin has an initial position  $x_0$  at the start of the first pulse ( $t = 0$ ), its displacement when measured at the beginning of the second pulse ( $t = \Delta$ ) is  $x = x_\Delta - x_0$ . Now, note the gradient can be set-up in any Cartesian direction. Hence, the diffusion gradient vector and spin displacement vectors are defined by,

$$\mathbf{G} = \begin{bmatrix} G_x \\ G_y \\ G_z \end{bmatrix}, \quad (3.4.1)$$



$$\mathbf{r} = \begin{bmatrix} x \\ y \\ z \end{bmatrix} = \begin{bmatrix} x_\Delta - x_0 \\ y_\Delta - y_0 \\ z_\Delta - z_0 \end{bmatrix}. \quad (3.4.2)$$

If the pulse duration  $\delta$  is infinitesimal, then by dimensional analysis the acquired phase in any direction is

$$\Delta\phi = \gamma\delta\mathbf{G} \cdot \mathbf{r}. \quad (3.4.3)$$

The magnetisation in the transverse direction was defined by Torrey (1956) to be

$$M_{xy} = M_x + iM_y, \quad (3.4.4)$$

with a signal proportional to its phase given by,

$$S \propto e^{i\phi}. \quad (3.4.5)$$

In §2.5, isotropic diffusion in the Fickian model was shown to be described by its corresponding PDF. If a single spin displaces along a Cartesian direction, then it emits a small signal

$$\delta S = S_0 \frac{1}{\sqrt{4\pi D\Delta}} e^{-\frac{\mathbf{r} \cdot \mathbf{r}}{4D\Delta}} e^{i\gamma\delta\mathbf{G} \cdot \mathbf{r}} \delta|\mathbf{r}|, \quad (3.4.6)$$

where  $S_0$  is the spin-echo signal without diffusion. So, the total signal is simply the integral of all signal contributions from the spin ensemble,

$$S = S_0 \frac{1}{\sqrt{4\pi D\Delta}} \int_{-\infty}^{\infty} e^{-\frac{\mathbf{r} \cdot \mathbf{r}}{4D\Delta}} e^{i\gamma\delta\mathbf{G} \cdot \mathbf{r}} d|\mathbf{r}|. \quad (3.4.7)$$

The details to solve this equation are omitted here but given by Mori (2007). The resulting isotropic signal equation is now expressed in a form first derived by Tanner and Stejskal (1965),

$$\ln\left(\frac{S}{S_0}\right) = -bD, \quad (3.4.8)$$

where  $b = \gamma^2 |\mathbf{G}|^2 \delta^2 (\Delta - \frac{\delta}{3})$ . The so-called  $b$ -factor is an operator-controlled parameter to scale the diffusion contrast of the image. It depends on the strength and timing of the pulses. A anisotropic signal equation is derived in a similar way to its counterpart. Equation 3.4.7 now transforms (Leow et al., 2009) to

$$S_j = S_0 \frac{1}{(4\pi\Delta)^{\frac{3}{2}} |\mathbf{D}|^{\frac{1}{2}}} \int_{-\infty}^{\infty} e^{-\frac{\mathbf{r}^T \mathbf{D}^{-1} \mathbf{r}}{4\Delta}} e^{i\gamma\delta\mathbf{G} \cdot \mathbf{r}} d\mathbf{r} \text{ for } j = x, y \text{ or } z. \quad (3.4.9)$$

This is a Fourier relationship with solution,

$$S_j = S_0 e^{-\mathbf{b}^T \mathbf{D} \mathbf{b}}, \quad (3.4.10)$$

where  $\mathbf{b} = \gamma^2 \mathbf{G}^2 \delta^2 (\Delta - \frac{\delta}{3})$  is the  $b$ -matrix.

Equations 3.4.8 and 3.4.10 are the basic signal equations of dMRI and are discussed further in §4.1.

# Introducing, comparing and contrasting popular imaging measures

## 4.1 Introducing some imaging measures of dMRI

### Mean diffusivity

Equation 3.4.8 is deceptive in its simplicity. It implies that only one pulse sequence is required to calculate  $D$  in a region of interest (ROI). However, consider a small volume of tissue (a voxel), Le Bihan et al. (1986) demonstrated that the detected water diffusion coefficient varies inside a voxel due to a number of factors, collectively known as intravoxel incoherent motions (IVIM).

To acknowledge IVIM, it is convention to change  $D$  to the apparent diffusion coefficient, ADC, an average of all three eigenvalues of  $\mathbf{D}$ . For reference, ADC will be referred to as the mean diffusivity, MD, from now on (Basser, 1995).

$$\text{MD} = \frac{\lambda_1 + \lambda_2 + \lambda_3}{3} \quad (4.1.1a)$$

$$= \frac{\lambda_x + \lambda_y + \lambda_z}{3} \quad (4.1.1b)$$

To calculate this value within an ROI, three orthogonal diffusion pulse sequences and one reference signal are required ( $b = 0$ ). The signal equations for a given Cartesian direction are a modified form of equation 3.4.8,

$$S_j = S_0 e^{-b\lambda_j} \text{ for } j = x, y \text{ or } z. \quad (4.1.2)$$

The signals are then multiplied together and the geometric mean is taken,

$$S_x S_y S_z = S_0^3 e^{-b(\lambda_x + \lambda_y + \lambda_z)}, \quad (4.1.3)$$

$$\sqrt[3]{S_x S_y S_z} = S_0 e^{-b(\frac{\lambda_x + \lambda_y + \lambda_z}{3})}, \quad (4.1.4)$$

$$S_{\text{DWI}} = S_0 e^{-b \cdot \text{MD}}, \quad (4.1.5)$$

where  $S_{\text{DWI}}$  is the signal of a diffusion weighted image (Mukherjee et al., 2008). A simple rearrangement for MD is now all that is required. By applying a pulse sequence four times for

each voxel, enough information can be acquired to form an MD image, because  $S_0$  and MD are the only unknowns. This measure is discussed in more detail in §4.2.

## Fractional anisotropy

Fractional anisotropy (FA) is an imaging measure calculated from the eigenvalues of  $\mathbf{D}$  (Basser, 1996),

$$\text{FA} = \sqrt{\frac{3}{2} \frac{\sqrt{(\lambda_1 - \text{MD})^2 + (\lambda_2 - \text{MD})^2 + (\lambda_3 - \text{MD})^2}}{\sqrt{\lambda_1^2 + \lambda_2^2 + \lambda_3^2}}}. \quad (4.1.6)$$

It quantitatively indicates the fraction of anisotropic diffusion within a voxel, between 0 and 1. Further introduction will be made in §4.2. For now, signal acquisition shall be briefly discussed. In order to obtain the matrix of eigenvalues from equation 2.3.3,  $\mathbf{D}$  must first be decoded from equation 3.4.10, by using the acquired diffusion signals. To simplify this process, recall from §2.4 that  $\mathbf{D}$  is assumed to be diagonally symmetric, i.e.  $D_{yx} = D_{xy}$ ,  $D_{zx} = D_{xz}$  and  $D_{zy} = D_{yz}$ . Signal acquisition is then made simpler, because there are now only six unknown non-collinear components (Huisman, 2010). So, for each voxel to be imaged, only six diffusion pulse sequences and one reference signal ( $b = 0$ ) are required. The diagonal elements of  $\mathbf{D}$  are found by activating an orthogonal diffusion gradient pulse (Mori, 2007). For example, if the  $x$ -direction gradient is activated, the exponent of equation 3.4.10 becomes,

$$\begin{aligned} \mathbf{b}^T \mathbf{D} \mathbf{b} &= \begin{bmatrix} b_x & 0 & 0 \end{bmatrix} \begin{bmatrix} D_{xx} & D_{xy} & D_{xz} \\ D_{yz} & D_{yy} & D_{yz} \\ D_{zx} & D_{zy} & D_{zz} \end{bmatrix} \begin{bmatrix} b_x \\ 0 \\ 0 \end{bmatrix}, \\ &= b_x^2 D_{xx}. \end{aligned} \quad (4.1.7)$$

$D_{xx}$  can then be calculated from all the other known terms. The off-diagonal elements of  $\mathbf{D}$  are found by activating any two orthogonal diffusion gradient pulses at once (Mori, 2007). For example, if the  $x$ -direction and  $y$ -direction gradients are activated, the exponent of equation 3.4.10 now becomes,

$$\begin{aligned} \mathbf{b}^T \mathbf{D} \mathbf{b} &= \begin{bmatrix} b_x & b_y & 0 \end{bmatrix} \begin{bmatrix} D_{xx} & D_{xy} & D_{xz} \\ D_{yz} & D_{yy} & D_{yz} \\ D_{zx} & D_{zy} & D_{zz} \end{bmatrix} \begin{bmatrix} b_x \\ b_y \\ 0 \end{bmatrix}, \\ &= b_x^2 D_{xx} + b_y^2 D_{yy} + 2b_x b_y D_{xy}. \end{aligned} \quad (4.1.8)$$

As before,  $D_{xy}$  can be found from all other known terms. This decoding process is repeated until all the elements of  $\mathbf{D}$  have been found. If the rotation matrix from Cartesian coordinates

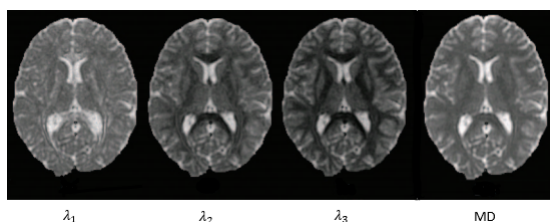
to the diffusion ellipsoid frame is known, the matrix of eigenvalues in equation 2.3.3 can be calculated (Rajagopalan et al., 2017). Subsequently, the eigenvalues and MD can be substituted into equation 4.1.6 to find the fractional anisotropy within a voxel. This process can be repeated for an entire region to form an image.

## 4.2 Comparing and contrasting imaging measures

### A pair of scalar dMRI measures

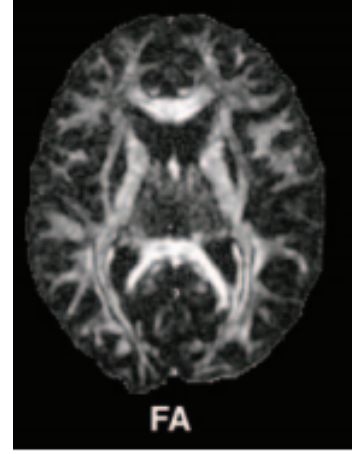
Mean diffusivity is a straight-forward scalar imaging measure. It is simply just an average of the eigenvalues obtained from orthogonal diffusion pulse sequences. Figure 4.1 shows this intuitively. The eigenvalues here are different due to their apparent diffusion in each direction. In this case,  $\lambda_1$  is markedly more different to  $\lambda_2$  and  $\lambda_3$ . It is thus reasonable to create an average, because a single image is much easier to interpret. Its role in accurate imaging diagnosis is discussed shortly.

Figure 4.1: Images corresponding to the three eigenvalues and their average. Credit to Mukherjee et al. (2008).



FA is also a scalar measure, but contrary to MD, shows the fraction of total diffusion in an ROI that has directional bias. In figure 4.2, FA displays only the magnitude of diffusion anisotropy and contains no vectorial information pertaining to the directions of motion. Traditionally, the anisotropy within an axon has been solely attributed to axial water diffusion (Beaulieu, 2001), owed to the tubular axon shape (refer to §2.4). Hence, it was reasonable to assume that a damaged axon will cause a proportionate increase in MD, as a response to a reduction in FA (Soares, 2013). Alegiani et al. (2017) has demonstrated that this assumption is incorrect in the case of acute ischemic stroke.

Figure 4.2: An FA map showing diffusion direction bias in the white brain matter tracts.  
Credit to Mukherjee et al. (2008).



In general, it is now well known that a reduction in FA can be caused by other factors. Possibilities include cell death and demyelination (Alba-Ferrara and de Erausquin, 2013; O'Donnell and Westin, 2011). This creates inaccuracy because the large ellipsoidal axon voxel cannot resolve between these differences. Therefore, great caution must be applied when attempting to meaningfully interpret an FA image. Despite its criticism, FA is particularly useful in detecting the onset of neurodegenerative disorders (Mole et al., 2016; Teipel et al., 2014).

## Introducing diffusion weighted imaging

$S_{\text{DWI}}$  in equation 4.1.5 is interpreted as a signal loss with respect to its reference,  $S_0$  (Jung and Weigel, 2013). This loss is attributed to the exponential diffusion term. In its absence,  $S_{\text{DWI}} = S_0$ , a simple spin-echo signal. In §3.3, it was stated that SS-EPI traverses all of  $k$ -space in one pulse. To make this possible, the echo train must be very long. In other words, the echo-time  $TE$  is great. Image resolution increases in proportion to the echo-time, but is constrained by the transverse magnetisation (Li et al., 2003). As shown in §3.2,  $M_{xy}$  tends towards zero. Hence, for long echo-times, the spin-echoes will attenuate until eventually they are too weak to be detected. However, this attenuation process is extended or reduced depending upon  $T_2$  within an ROI (figure 3.5). SS-EPI is thus said to be  $T_2$ -weighted.

Now consider equation 4.1.5,  $S_0$  can be substituted for its transverse magnetisation factor,

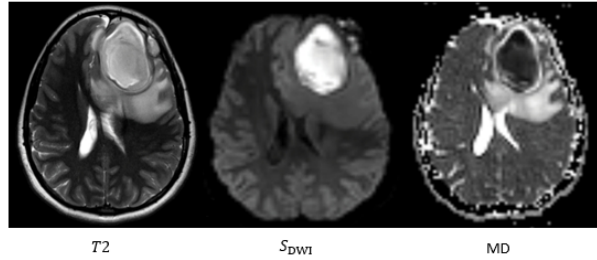
$$S_{\text{DWI}} = ke^{-\frac{TE}{T_2}} e^{-b \cdot \text{MD}}, \quad (4.2.1)$$

where  $k$  is a proportionality constant. On inspection of this equation, areas within images created from the diffusion-weighted signal alone will shine brightly if the imaged region has

high  $T2$  or low MD (Mukherjee et al., 2008). The latter corresponds to a diffusion restriction within an ROI and has many pathological causes (Finelli, 2012). Differentiation between the so-called  $T2$  shine-through artifact and diffusion restriction is thus vital for accurate diagnosis.

Mean diffusivity is a very important measure for disease confirmation. Refer back to equation 4.2.1 and note that  $S_{DWI}$  and MD share an inversely proportional relationship. Hence, for restricted diffusion, the bright regions of a  $S_{DWI}$  image will turn dark in an MD image. If the MD image is unchanged, then the bright signal in the  $S_{DWI}$  image might be a consequence of  $T2$  shine-through (Albano et al., 2016). This is confirmed with a  $T2$ -weighted image. Figure 4.3 shows the triplet of images used to confirm restricted diffusion. This conglomerate diagnostic procedure is normally referred to as diffusion-weighted imaging (DWI). This procedure is robust and accurate. It is held in high regard for early stroke detection (Bang and Li, 2019). Unfortunately, FA cannot match this standard because it does not share a time dependency with the onset of stroke (Alegiani et al., 2017).

Figure 4.3: Restricted isotropic diffusion caused by a frontal and epidural brain abscess. Credit to Huisman (2010).



## Assigning voxel-wise direction

The eigenvalue of greatest magnitude in  $\mathbf{\Lambda}$  (refer to equation 2.3.3), identifies the principal (axial) direction of the ellipsoidal axon voxel and its orientation in the scanner frame. If a large set of axial eigenvalues are obtained from an ROI, the connectivity can be ascertained by joining the voxels together by their principal directions (Huisman, 2010). Thus creating a model that represents the axon bundles of white brain matter.

To add information about three-dimensional diffusion flow along these connected regions, the axial eigenvalues are assigned a colour in an anatomical coordinate system. Green is left to right, red is anterior to posterior and blue is inferior to superior (O'Donnell and Westin, 2011). Angular flow in this coordinate system is simply represented by mixed colours. These coloured ellipsoids are known as glyphs (O'Donnell and Westin, 2011). The FA for each glyph is simply the intensity of its colour. This form of imaging is an advanced technique known as

DTI tractography. Figure 4.4 shows a magnified region of white brain matter represented by a glyph map, and figure 4.5, the coloured fractional anisotropy (cFA) map.

Figure 4.4: Coloured ellipsoids (glyphs) show a representation of the anisotropic diffusion flow and its magnitude in a region. Credit to O'Donnell and Westin (2011).

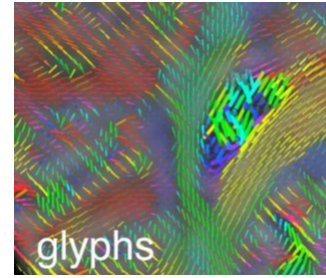
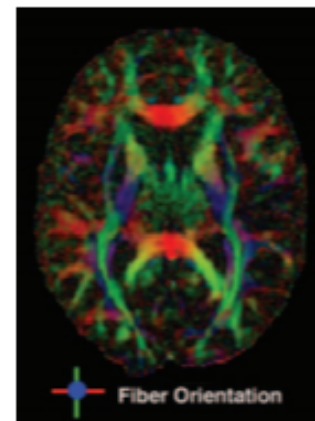


Figure 4.5: A coloured fractional anisotropy map. Credit to Mukherjee et al. (2008).



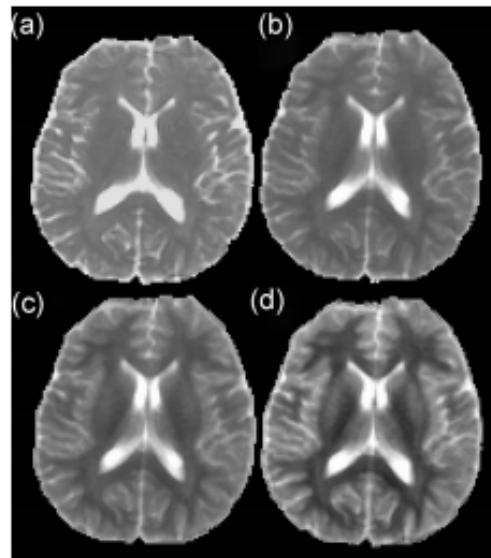
The main benefit of DTI tractography is the level of information it yields over FA and MD. Despite its level of advancement, caution should be applied when attempting to interpret the image. When ellipsoidal voxels are not aligned, their combination results in a reduction in FA (Feldman et al., 2010). This disrupts the connectivity that the model is attempting to represent. Therefore, the axon pathways shown in the cFA image could be inaccurate (Soares et al., 2013). Nevertheless, it has still found its use as a medical tool (Sedrak et al., 2019) and enhances scalar FA in some applications (Pan et al., 2016). Moreover, its technological requirements are slim when compared to Q-Ball imaging (Tuch, 2004).

# General considerations to improve accuracy

## 5.1 Optimising the $b$ -value

In §3.4, it was mentioned that the  $b$ -value is a factor used to scale diffusion contrast. More accurately,  $b$  is responsible for controlling the intensity of  $T2$  shine-through in an image. Figure 5.1 shows this effect. There is some guidance about the usage of optimum  $b$ -values to assist in the diagnosis of various diseases (Bonekamp et al., 2012). However, a previous study has shown that these values may vary in MD according to signal-to-noise (SNR), and contrast-to-noise (CNR) in FA (Kingsley and Monahan, 2004). Scanners of weaker  $B_0$  can have their SNR differ by as much as 15% between 1.5 T and 3 T (Polders et al., 2011). This would be further exacerbated in FA, because tensor imaging contrast is dependent upon the SNR of its 6 component images. So, in general, there are no clear-cut  $b$ -values (Jones and Cercignani, 2010). It is my recommendation to the operator to find the right balance of  $T2$  shine-through, within the proximity of an optimum value.

Figure 5.1:  $T2$  shine-through becomes progressively brighter as  $b$  increases. a.  $b = 1000 \text{ s mm}^{-2}$ ; b.  $b = 2000 \text{ s mm}^{-2}$ ; c.  $b = 3000 \text{ s mm}^{-2}$ ; d.  $b = 4000 \text{ s mm}^{-2}$ . Credit to Jones and Cercignani, 2010.





## 5.2 Magnetic field strength and SNR

Studies have shown that the SNR of a dMRI image increases proportionality with respect to the main magnetic field. Indeed, a relative increase in SNR of 3.2 is possible by increasing the field strength from 1.5 T to 7.0 T (Polders et al., 2011). This is because the magnetisation of protons within water molecules is directly proportional to  $\mathbf{B}_0$ ,

$$\mathbf{M} = \frac{\chi \mathbf{B}_0}{\mu_0}, \quad (5.2.1)$$

where  $\mu_0$  is the permeability of free space and  $\chi$  is the magnetic susceptibility. SNR can also be improved by increasing its NEX (number of excitations), i.e. by obtaining more than one diffusion signal per voxel, by repeating the pulse sequence (Farrell et al., 2007). Increasing NEX does unfortunately have the disadvantage of raising total scan time. So a reduced amount of NEX can be compensated with operator experience, in order to obtain an equal balance of image accuracy and scan time (Soman et al., 2014). It is well known that low SNR increases FA bias in images, creating the potential for inaccurate diagnosis (Farrell et al., 2007). Therefore, high SNR should always be a priority.

## 5.3 Increasing gradient pulse angular resolution

High angular resolution diffusion imaging (HARDI) is an advanced technique which increases the number of diffusion pulses in DTI from six to 64 (Berman et al., 2013). This technique greatly improves the accuracy of FA and DTI tractography by allowing intra-voxel imaging and advanced fibre tracking. Thus, it helps to resolve intra-voxel reductions in FA as mentioned before in §4.2. A further study has shown that only 32 pulses need to be applied for optimal FA accuracy and precision of repeated measurements (Liu et al., 2013). MD also benefits by showing an improvement in its precision with only 15 applied pulses required. DTI tractography should always be used with HARDI.

# Conclusion

In this report, diffusion and MRI have been covered at length. Beginning humbly with Fick's laws, isotropic and anisotropic diffusion have been described and modelled by solving his equations. Magnetic resonance was then explained to be a response of its magnetisation vector to an RF pulse. In particular, a  $90^\circ$ - $180^\circ$  pulse is a special type of sequence required for dMRI, known as the spin-echo. Coupling the diffusion pulses with the SS-EPI sequence and using the probability density functions solved from Fick's second law, signal equations for diffusion isotropy and anisotropy were derived. Subsequently, two popular measures were described from the eigenvalues of the diffusion tensor.

Mean diffusivity is often used as a tool to confirm diffusion restriction. Studies have shown that it is a robust and accurate technique for the early detection of stroke. Fractional anisotropy, despite its intrinsic inaccuracy shown in studies, can be useful for the early detection of neurodegenerative diseases.

The following recommendations should be followed for optimum dMRI imaging accuracy as detailed in this report:

1. The pulse sequence type should always be of rapid acquisition for reduced noise due to motion. SS-EPI is a robust technique to complete this.
2. Bright regions inside  $S_{\text{DWI}}$  images must always be checked with MD images to avoid misdiagnosis due to  $T2$  shine-through.
3. FA images should always be carefully interpreted by the operator due to intrinsic inaccuracies. A reduction in FA may not be solely due to axon damage.
4. A clear-cut  $b$ -value is not defined. Instead, the operator must adjust the scanner settings with best judgment and refer to literature to find the optimum value.
5. A scanner with high  $\mathbf{B}_0$  is always preferred to increase SNR, thus reducing FA bias that may lead to inaccuracy. If a high field scanner is not available, the operator should consider increasing NEX.

6. If high angular resolution is available on the scanner, the number of pulses should be set to at least 32 for optimum FA accuracy and precision. MD should be set to 15 if multiple images of one region are required. DTI tractography should always be used with HARDI if possible.

Word count - 4900 words

# References

- [1] Einstein, A. (1905) ‘Über die von der molekularkinetischen Theorie der Wärme geforderte Bewegung von in ruhenden Flüssigkeiten suspendierten Teilchen’, *Annalen der Physik*, vol. 322, no. 8, pp. 549-560 [Online]. Available at <https://doi.org/10.1002/andp.19053220806> (Accessed 02 July 2019).
- [2] Fick, A. (1855) ‘Ueber Diffusion’, *Annalen der Physik*, vol. 170, no. 1, pp. 59-86 [Online]. Available at <https://doi.org/10.1002/andp.18551700105> (Accessed 02 July 2019).
- [3] Plewes, D. B., Kucharczyk, W. (2012) ‘Physics of MRI: A primer’, *Journal of Magnetic Resonance Imaging*, vol. 35, no. 5, pp. 1038-1054 [Online]. Available at <https://doi.org/10.1002/jmri.23642> (Accessed 14 March 2019).
- [4] Huisman, T.A.G.M. (2010) ‘Diffusion-weighted and diffusion tensor imaging of the brain, made easy’, *Cancer Imaging*, vol. 10, no. 1A, pp. 163-171 [Online]. Available at <https://www.doi.org/10.1102/1470-7330.2010.9023> (Accessed 16 August 2019).
- [5] Sakka, L., Coll, G., Chazal, J. (2011) ‘Anatomy and physiology of cerebrospinal fluid’, *European Annals of Otorhinolaryngology, Head and Neck Diseases*, vol. 128, no. 6, pp. 283-334 [Online]. Available at <https://doi.org/10.1016/j.anorl.2011.03.002> (Accessed 22 August 2019).
- [6] Crichton, R., Ward, R. (2013) *Metal-Based Neurodegeneration: From Molecular Mechanisms to Therapeutic Strategies* [Online], Chichester, John Wiley and Sons, Inc. Available at <https://www.doi.org/10.1002/9781118553480.ch01> (Accessed 19 August 2019).
- [7] Reiser, M.F., Semmler, W., Hricak, H. (2008) *Magnetic Resonance Tomography* [Online], Berlin, Springer. Available at <https://www.doi.org/10.1007/978-3-540-29355-2> (Accessed 19 August 2019).
- [8] Tournier, J-D. (2019) ‘Diffusion MRI in the brain – Theory and concepts’, *Progress in Nuclear Magnetic Resonance Spectroscopy*, vol. 112-113, no. 1, pp. 1-16 [Online]. Available at <https://doi.org/10.1016/j.pnmrs.2019.03.001> (Accessed 14 March 2019).

- [9] Moseley, M. E., Kucharczyk, J., Asgari, H. S., Norman, D. (1991) ‘Anisotropy in diffusion-weighted MRI’, *Magnetic Resonance in Medicine*, vol. 19, no. 2, pp. 321-326 [Online]. Available at <https://doi.org/10.1002/mrm.1910190222> (Accessed 22 August 2019).
- [10] Crank, J. (1975) *The Mathematics of Diffusion*, 2nd edn, London, Oxford University Press.
- [11] Bassar, P.J., Mattiello, J., LeBihan, D. (1994) ‘MR diffusion tensor spectroscopy and imaging’, *Biophysical Journal*, vol. 66, no. 1, pp. 259-267 [Online]. Available at [https://www.doi.org/10.1016/S0006-3495\(94\)80775-1](https://www.doi.org/10.1016/S0006-3495(94)80775-1) (Accessed 10 August 2019).
- [12] Balluffi, R.W., Allen, S.M., Carter, W.C. (2005) *Kinetics of Materials* [Online], New Jersey, John Wiley and Sons, Inc. Available at <https://www.doi.org/10.1002/0471749311> (Accessed 12 August 2019).
- [13] Harville, D. (2018) *Linear Models and the Relevant Distributions and Matrix Algebra* [Online], New York, Chapman and Hall/CRC. Available at <https://doi-org.libezproxy.open.ac.uk/10.1201/9781351264686> (Accessed 10 August 2019).
- [14] Hahn, E.L. (1950a) ‘Nuclear Induction Due to Free Larmor Precession’, *Physical Review*, vol. 77, no. 2, pp. 297-298 [Online]. Available at <https://www.doi.org/10.1103/PhysRev.77.297.2> (Access 15 August 2019).
- [15] Bloch, F. (1946) ‘Nuclear Induction’, *Physical Review*, vol. 70, no. 7-8, pp. 460-474 [Online]. Available at <https://www.doi.org/10.1103/PhysRev.70.460> (Accessed 10 August 2019).
- [16] Hahn, E. L. (1950b) ‘Spin Echoes’, *Physical Review*, vol. 80, no. 4, pp. 580-594 [Online]. Available at <https://www.doi.org/10.1103/PhysRev.80.580> (Accessed 08 August 2019).
- [17] Neil, J. J. (1997) ‘Measurement of water motion (apparent diffusion) in biological systems’, *Concepts in Magnetic Resonance*, vol. 9, no. 6, pp. 385-401 [Online]. Available at [https://doi.org/10.1002/\(SICI\)1099-0534\(1997\)9:6<385::AID-CMR2>3.0.CO;2-V](https://doi.org/10.1002/(SICI)1099-0534(1997)9:6<385::AID-CMR2>3.0.CO;2-V) (Accessed 26 August 2019).

- [18] Huang, S. Y., Seethamraju, R. T., Patel, P., Hahn, P. F., Kirsch, J. E., Guimaraes, A. R. (2015) ‘Body MR Imaging: Artifacts, k-Space and Solutions’, *RadioGraphics*, vol. 35, no. 5, pp. 1439-1460 [Online]. Available at <https://doi.org/10.1148/rg.2015140289> (Accessed 28 August 2019).
- [19] Stehling, M. K., Turner, R., Mansfield, P. (1991) ‘Echo-planar imaging: magnetic resonance imaging in a fraction of a second’, *Science*, vol. 254, no. 5028, pp. 43-50 [Online]. Available at <https://doi.org/10.1126/science.1925560> (Accessed 11 April 2019).
- [20] Brown, R. W., Cheng, Y. N., Haacke, E. M., Thompson, M. R., Venkatesan, R. (2014) *Magnetic Resonance Imaging* [Online], New Jersey, John Wiley and Sons, Inc. Available at <https://www.doi.org/10.1002/9781118633953> (Accessed 28 August 2019).
- [21] Torrey, H. C. (1956) ‘Bloch Equations with Diffusion Terms’, *Physical Review*, vol. 104, no. 3, pp. 563-565 [Online]. Available at <https://www.doi.org/10.1103/PhysRev.104.563> (Accessed 10 August 2019).
- [22] Tanner, J. E., Stejskal, E. O. (1965) ‘Spin Diffusion Measurements: Spin Echoes in the Presence of a Time-Dependent Field Gradient’, *Journal of Chemical Physics*, vol. 42, no. 1, pp. 288-292 [Online]. Available at <https://doi.org/10.1063/1.1695690> (Accessed 11 April 2019).
- [23] Alexander, A. L., Tsuruda, J. S., Parker, D. L. (2006) ‘Elimination of eddy current artifacts in diffusion-weighted echo-planar images: The use of bipolar gradients’, *Magnetic Resonance in Medicine*, vol. 38, no. 6, pp. 1016-1021 [Online]. Available at <https://doi.org/10.1002/mrm.1910380623> (Accessed 28 August 2019).
- [24] Mori, S. (2007) *Introduction to Diffusion Tensor Imaging* [Online], Amsterdam, Elsevier Science and Technology. Available at <https://www.doi.org/10.1016/C2011-0-07607-X> (Accessed 20 August 2019).
- [25] Leow, A. D., Zhu, S., Zhan, L., McMahon, K., de Zubicaray, G. I., Meredith, M., Wright, M. J., Toga, A. W., Thompson, P. M. (2009) ‘The Tensor Distribution Function’, *Magnetic Resonance in Medicine*, vol. 61, no. 1, pp. 205-214 [Online]. Available at <https://doi.org/10.1002/mrm.21852> (Accessed 20 August 2019).

- [26] Mukherjee, P., Berman, J. I., Chung, S. W., Hess, C. P., Henry, R. G. (2008) ‘Diffusion Tensor MR Imaging and Fiber Tractography: Theoretic Underpinnings’, *American Journal of Neuroradiology*, vol. 29, no. 4, pp. 632-641 [Online]. Available at <https://doi.org/10.3174/ajnr.A1051> (Accessed 24 August 2019).
- [27] Le Bihan, D., Breton, E., Lallemand, D., Grenier, P., Cabanis, E., Laval-Jeantet, M. (1986) ‘MR Imaging of Intravoxel Incoherent Motions: Application to Diffusion and Perfusion in Neurologic Disorders’, *Radiology*, vol. 161, no. 2, pp. 401-407 [Online]. Available at <https://www.doi.org/10.1148/radiology.161.2.3763909> (Accessed 29 August 2019).
- [28] Basser, P. (1995) ‘Inferring Microstructural Features and the Physiological State of Tissues from Diffusion Weighted Images’, *NMR In Biomedicine*, vol. 8, no. 7, pp. 333-344 [Online]. Available at <https://doi.org/10.1002/nbm.1940080707> (Accessed 28 August 2019).
- [29] Rajagopalan, V., Jiang, Z., Stojanovic-Radic, J., Yue, G. H., Pioro, E.P., Wylie, G.R., Das, A. (2017) ‘A Basic Introduction to Diffusion Tensor Imaging Mathematics and Image Processing Steps’, *Brain Disorders and Therapy*, vol. 6, no. 2 [Online]. Available at <https://www.doi.org/10.4172/2168-975X.1000229> (Accessed 16 August 2019).
- [30] Basser, P. J., Pierpaoli, C. (1996) ‘Microstructural and physiological features of tissues elucidated by quantitative-diffusion-tensor MRI’, *Journal of Magnetic Resonance*, vol. 111, no. 3, pp. 209-219 [Online]. Available at <https://doi.org/10.1006/jmrb.1996.0086> (Accessed 31 August 2019).
- [31] Basser, P. J., Pajevic, S. (2000) ‘Statistical Artifacts in Diffusion Tensor MRI (DT-MRI) Caused by Background Noise’, *Magnetic Resonance in Medicine*, vol. 44, no. 1, pp. 41-50 [Online]. Available at [https://doi.org/10.1002/1522-2594\(200007\)44:1;1::AID-MRM8;3.0.CO;2-O](https://doi.org/10.1002/1522-2594(200007)44:1;1::AID-MRM8;3.0.CO;2-O) (Accessed 18 August 2019).
- [32] Kingsley, P. B., Monahan, W. G. (2004) ‘Selection of the Optimum b factor for Diffusion-Weighted Magnetic Resonance Imaging Assessment of Ischemic Stroke’, *Magnetic Resonance in Medicine*, vol. 51, no. 5, pp. 996-1001 [Online]. Available at <https://doi.org/10.1002/mrm.20059> (Accessed 02 August 2019).

- [33] Bonekamp, S., Corona-Villalobos, C. P., Kamel, I. R. (2012) ‘Oncologic Applications of Diffusion-Weighted MRI in the Body’, *Journal of Magnetic Resonance Imaging*, vol. 35, no. 2, pp. 257-279 [Online]. Available at <https://doi.org/10.1002/jmri.22786> (Accessed 19 August 2019).
- [34] Finelli, P. F. (2012) ‘Diagnostic approach to restricted-diffusion patterns on MR imaging’, *Neurology Clinical Practice*, vol. 2, no. 4, pp. 287-293 [Online]. Available at <https://www.doi.org/10.1212/CPJ.0b013e318278bee1> (Accessed 26 August 2019).
- [35] Polders, D. L., Leemans, A., Hendrikse, J., Donahue, M. J., Luijten, P. R., Hoogduin, J. M. (2011) ‘Signal to Noise Ratio and Uncertainty in Diffusion Tensor Imaging at 1.5, 3.0, and 7.0 Tesla’, *Journal of Magnetic Resonance Imaging*, vol. 33, no. 6, pp. 1456-1463 [Online]. Available at <https://doi.org/10.1002/jmri.22554> (Accessed 24 August 2019).
- [36] Bang, O. Y., Li, W. (2019) ‘Applications of diffusion-weighted imaging in diagnosis, evaluation, and treatment of acute ischemic stroke’, *Precision and Future Medicine*, vol. 3, no. 2, pp. 69-76 [Online]. Available at <https://doi.org/10.23838/pfm.2019.00037> (Accessed 17 August 2019).
- [37] Jung, B. A., Weigel, M. (2013) ‘Spin Echo Magnetic Resonance Imaging’, *Journal of Magnetic Resonance Imaging*, vol. 37, no. 4, pp. 805-817 [Online]. Available at <https://doi.org/10.1002/jmri.24068> (Accessed 10 August 2019).
- [38] Li, T., Mirowitz, S. A. (2003) ‘Fast T2-weighted MR imaging: impact of variation in pulse sequence parameters on image quality and artifacts’, *Magnetic Resonance Imaging*, vol. 21, no. 7, pp. 745-753 [Online]. Available at [https://doi.org/10.1016/S0730-725X\(03\)00173-5](https://doi.org/10.1016/S0730-725X(03)00173-5) (Accessed 20 August 2019).
- [39] Mole, J. P., Subramanian, L., Bracht, T., Morris, H., Metzler-Baddeley, C., Linden, D. E. J. (2016) ‘Increased fractional anisotropy in the motor tracts of Parkinson’s disease suggests compensatory neuroplasticity or selective neurodegeneration’, *European Radiology*, vol. 26, no. 10, pp. 3327-3335 [Online]. Available at <https://www.doi.org/10.1007/s00330-015-4178-1> (Accessed 21 August 2019).



- [40] Teipel, S. J., Grothe, M. J., Filippi, M., Fellgiebel, A., Dyrba, M., Frisoni, G. B., Meindl, T., Bokde, A. L., Hampel, H., Kloppel, S., Hauenstein, K. (2014) ‘Fractional anisotropy changes in Alzheimer’s disease depend on the underlying fiber tract architecture: a multiparametric DTI study using joint independent component analysis.’, *Journal of Alzheimer’s Disease*, vol. 41, no. 1, pp. 69-83 [Online]. Available at <https://doi.org/10.3233/JAD-131829> (Accessed 21 August 2019).
- [41] Jones, D. K., Cercignani, M. (2010) ‘Twenty-five pitfalls in the analysis of diffusion MRI data’, *NMR in Biomedicine*, vol. 23, no. 7, pp. 803-820 [Online]. Available at <https://www.doi.org/10.1002/nbm.1543> (Accessed 05 August 2019).
- [42] Beaulieu, C. (2002) ‘The basis of anisotropic water diffusion in the nervous system – a technical review’, *NMR in Biomedicine*, vol. 15, no. 7-8, pp. 435-455 [Online]. Available at <https://www.doi.org/10.1002/nbm.782> (Accessed 19 August 2019).
- [43] Alba-Ferrara, L. M., de Erausquin, G. A. (2013) ‘What does anisotropy measure? Insights from increased and decreased anisotropy in selective fiber tracts in schizophrenia’, *Frontiers in Integrative Neuroscience*, vol. 7, no. 1 [Online]. Available at <https://doi.org/10.3389/fnint.2013.00009> (Accessed 18 August 2019).
- [44] O’Donnell, L. J., Westin, C-F. (2011) ‘An Introduction to Diffusion Tensor Image Analysis’, *Neurosurgery Clinics of North America*, vol. 22, no. 2, pp. 185-196 [Online]. Available at <https://doi.org/10.1016/j.nec.2010.12.004> (Accessed 20 August 2019).
- [45] Pan, E., Mehmet, A. A., Ates, A., Algul, A., Aytekin, A., Basoglu, C., Ebrinc, S., Cetin, M., Kose, S. (2016) ‘Fractional Anisotropic Changes of Corpus Callosum Associated with Antipsychotic Treatment in First-Episode Antipsychotic Drug-Naive Patients with Schizophrenia’, *Klinik Psikofarmakoloji Bülteni-Bulletin of Clinical Psychopharmacology*, vol. 26, no. 4, pp. 332-341 [Online]. Available at <https://doi.org/10.5455/bcp.20160319021659> (Accessed 22 August 2019).
- [46] Sedrak, M., Gorgulho, A., Bari, A., Behnke, E., Frew, A., Gevorkyan, I., Pouratian, N., DeSalles, A. (2010) ‘Diffusion tensor imaging (DTI) and colored fractional anisotropy (FA) mapping of the subthalamic nucleus (STN) and the globus pallidus interna (GPi)’, *Acta Neurochirurgica*, vol. 152, no. 12, pp. 2079-2084 [Online]. Available at <https://www.doi.org/10.1007/s00701-010-0813-4> (Accessed 22 August 2019).

- [47] Tuch, D. S. (2004) ‘Q-ball imaging’, *Magnetic Resonance in Medicine*, vol. 52, no. 6, pp. 1358-1372 [Online]. Available at <https://doi.org/10.1002/mrm.20279> (Accessed 24 August 2019).
- [48] Liu, X., Yang, Y., Sun, J., Yu, G., Xu, J., Niu, C., Tian, H., Lin, P. (2014) ‘Reproducibility of diffusion tensor imaging in normal subjects: an evaluation of different gradient sampling schemes and registration algorithm’, *Functional Neuroradiology*, vol. 56, no. 6, pp. 497-510 [Online]. Available at <https://www.doi.org/10.1007/s00234-014-1342-2> (Accessed 16 August 2019).
- [49] Polders, D. L., Leemans, A., Hendrikse, J., Donahue, M. J., Luijten, P. R., Hoogduin, J. M. (2011) ‘Signal to Noise Ratio and Uncertainty in Diffusion Tensor Imaging at 1.5, 3.0, and 7.0 Tesla’, *Journal of Magnetic Resonance Imaging*, vol. 33, no. 6, pp. 1456-1463 [Online]. Available at <https://doi.org/10.1002/jmri.22554> (Accessed 24 August 2019).
- [50] Farrell, J. A. D., Landman, B. A., Jones, C. K., Smith, S. A., Prince, J. L., van Zijl, P. C. M. (2007) ‘Effects of Signal-to-Noise Ratio on the Accuracy and Reproducibility of Diffusion Tensor Imaging – Derived Fractional Anisotropy, Mean Diffusivity, and Principal Eigenvector Measurements at 1.5T’, *Journal of Magnetic Resonance Imaging*, vol. 26, no. 3, pp. 756-767 [Online]. Available at <https://doi.org/10.1002/jmri.21053> (Accessed 17 August 2019).
- [51] Soman, S., Holdsworth, S. J., Skare, S., Andre, J. B., Van, A. T., Aksoy, M., Bammer, R., Rosenberg, J., Barnes, P. D., Yeom, K. W. (2014) ‘Effect of Number of Acquisitions in Diffusion Tensor Imaging of the Pediatric Brain: Optimizing Scan Time and Diagnostic Experience’, *Journal of Neuroimaging*, vol. 25, no. 2, pp. 296-302 [Online]. Available at <https://doi.org/10.1111/jon.12093> (Accessed 21 August 2019).
- [52] Berman, J. I., Lanza, M. R., Blaskey, L., Edgar, J. C., Roberts, T. P. L. (2013) ‘High Angular Resolution Diffusion Imaging (HARDI) Probabilistic Tractography of the Auditory Radiation’, *American Journal of Neuroradiology*, vol. 34, no. 8, pp. 1573-1578 [Online]. Available at <https://doi.org/10.3174/ajnr.A3471> (Accessed 21 August 2019).